Available online at www.sciencedirect.com

ScienceDirect

Advances in Space Research 74 (2024) 4353–4367

ADVANCES IN SPACE RESEARCH (a COSPAR publication)

www.elsevier.com/locate/asr

The Calorimetric Electron Telescope (CALET) on the International Space Station: Results from the first eight years on orbit

Y. Akaike [a,b,*], O. Adriani [c,d], K. Asano [e], Y. Asaoka [e], E. Berti [d,f], G. Bigongiari [g,h], W.R. Binns [i], M. Bongi [c,d], P. Brogi [g,h], A. Bruno [j], N. Cannady [k,l,m], G. Castellini [f], C. Checchia [g,h], M.L. Cherry [n], G. Collazuol [o,p], G.A. de Nolfo [j], K. Ebisawa [q], A.W. Ficklin [n], H. Fuke [q], S. Gonzi [c,d,f], T.G. Guzik [n], T. Hams [k], K. Hibino [r], M. Ichimura [s], W. Ishizaki [e], M.H. Israel [i], K. Kasahara [t], J. Kataoka [u], R. Kataoka [v], Y. Katayose [w], C. Kato [x], N. Kawanaka [y,z], Y. Kawakubo [n], K. Kobayashi [a,b], K. Kohri [y,aa], H.S. Krawczynski [i], J.F. Krizmanic [l], P. Maestro [g,h], P.S. Marrocchesi [g,h], A.M. Messineo [h,ab], J.W. Mitchell [l], S. Miyake [ac], A.A. Moiseev [ad,l,m], M. Mori [ae], N. Mori [d], H.M. Motz [r], K. Munakata [x], S. Nakahira [q], J. Nishimura [q], M. Negro [n], S. Okuno [r], J.F. Ormes [af], S. Ozawa [ag], L. Pacini [d,f], P. Papini [d], B.F. Rauch [i], S.B. Ricciarini [d,f], K. Sakai [k,l,m], T. Sakamoto [ah], M. Sasaki [ad,l,m], Y. Shimizu [r], A. Shiomi [ai], P. Spillantini [c], F. Stolzi [g,h], S. Sugita [ah], A. Sulaj [g,h], M. Takita [e], T. Tamura [r], T. Terasawa [e], S. Torii [a], Y. Tsunesada [aj,ak], Y. Uchihori [al], E. Vannuccini [d], J.P. Wefel [n], K. Yamaoka [am], S. Yanagita [an], A. Yoshida [ah], K. Yoshida [t], W.V. Zober [i]

[a] *Waseda Research Institute for Science and Engineering, Waseda University, 17 Kikuicho, Shinjuku, Tokyo 162-0044, Japan*
[b] *JEM Utilization Center, Human Spaceflight Technology Directorate, Japan Aerospace Exploration Agency, 2-1-1 Sengen, Tsukuba, Ibaraki 305-8505, Japan*
[c] *Department of Physics, University of Florence, Via Sansone, 1 - 50019, Sesto Fiorentino, Italy*
[d] *INFN Sezione di Firenze, Via Sansone, 1 - 50019, Sesto Fiorentino, Italy*
[e] *Institute for Cosmic Ray Research, The University of Tokyo, 5-1-5 Kashiwa-no-Ha, Kashiwa, Chiba 277-8582, Japan*
[f] *Institute of Applied Physics (IFAC), National Research Council (CNR), Via Madonna del Piano, 10, 50019, Sesto Fiorentino, Italy*
[g] *Department of Physical Sciences, Earth and Environment, University of Siena, via Roma 56, 53100 Siena, Italy*
[h] *INFN Sezione di Pisa, Polo Fibonacci, Largo B. Pontecorvo, 3 - 56127 Pisa, Italy*
[i] *Department of Physics and McDonnell Center for the Space Sciences, Washington University, One Brookings Drive, St. Louis, MO 63130-4899, USA*
[j] *Heliospheric Physics Laboratory, NASA GSFC, Greenbelt, MD 20771, USA*
[k] *Center for Space Sciences and Technology, University of Maryland, Baltimore County, 1000 Hilltop Circle, Baltimore, MD 21250, USA*
[l] *Astroparticle Physics Laboratory, NASA GSFC, Greenbelt, MD 20771, USA*
[m] *Center for Research and Exploration in Space Sciences and Technology, NASA GSFC, Greenbelt, MD 20771, USA*
[n] *Department of Physics and Astronomy, Louisiana State University, 202 Nicholson Hall, Baton Rouge, LA 70803, USA*
[o] *Department of Physics and Astronomy, University of Padova, Via Marzolo, 8, 35131 Padova, Italy*
[p] *INFN Sezione di Padova, Via Marzolo, 8, 35131 Padova, Italy*
[q] *Institute of Space and Astronautical Science, Japan Aerospace Exploration Agency, 3-1-1 Yoshinodai, Chuo, Sagamihara, Kanagawa 252-5210, Japan*
[r] *Kanagawa University, 3-27-1 Rokkakubashi, Kanagawa, Yokohama, Kanagawa 221-8686, Japan*
[s] *Faculty of Science and Technology, Graduate School of Science and Technology, Hirosaki University, 3, Bunkyo, Hirosaki, Aomori 036-8561, Japan*

* Corresponding author at: Waseda Research Institute for Science and Engineering, Waseda University, 17 Kikuicho, Shinjuku, Tokyo 162-0044, Japan.
E-mail address: yakaike@aoni.waseda.jp (Y. Akaike).

https://doi.org/10.1016/j.asr.2024.04.035

[t] Department of Electronic Information Systems, Shibaura Institute of Technology, 307 Fukasaku, Minuma, Saitama 337-8570, Japan
[u] School of Advanced Science and Engineering, Waseda University, 3-4-1 Okubo, Shinjuku, Tokyo 169-8555, Japan
[v] National Institute of Polar Research, 10-3, Midori-cho, Tachikawa, Tokyo 190-8518, Japan
[w] Faculty of Engineering, Division of Intelligent Systems Engineering, Yokohama National University, 79-5 Tokiwadai, Hodogaya, Yokohama 240-8501, Japan
[x] Faculty of Science, Shinshu University, 3-1-1 Asahi, Matsumoto, Nagano 390-8621, Japan
[y] National Astronomical Observatory of Japan, 2-21-1 Osawa, Mitaka, Tokyo 181-8588, Japan
[z] Department of Physics, Graduate School of Science, Tokyo Metropolitan University, 1-1, Minamii-Osawa, Hachijoji, Tokyo 192-0397, Japan
[aa] Institute of Particle and Nuclear Studies, High Energy Accelerator Research Organization, 1-1 Oho, Tsukuba, Ibaraki 305-0801, Japan
[ab] University of Pisa, Polo Fibonacci, Largo B. Pontecorvo, 3 - 56127 Pisa, Italy
[ac] Department of Electrical and Electronic Systems Engineering, National Institute of Technology (KOSEN), Ibaraki College, 866 Nakane, Hitachinaka, Ibaraki 312-8508, Japan
[ad] Department of Astronomy, University of Maryland, College Park, MD 20742, USA
[ae] Department of Physical Sciences, College of Science and Engineering, Ritsumeikan University, Shiga 525-8577, Japan
[af] Department of Physics and Astronomy, University of Denver, Physics Building, Room 211, 2112 East Wesley Avenue, Denver, CO 80208-6900, USA
[ag] Quantum ICT Advanced Development Center, National Institute of Information and Communications Technology, 4-2-1 Nukui-Kitamachi, Koganei, Tokyo184-8795, Japan
[ah] College of Science and Engineering, Department of Physics and Mathematics, Aoyama Gakuin University, 5-10-1 Fuchinobe, Chuo, Sagamihara, Kanagawa 252-5258, Japan
[ai] College of Industrial Technology, Nihon University, 1-2-1 Izumi, Narashino, Chiba 275-8575, Japan
[aj] Graduate School of Science, Osaka Metropolitan University, Sugimoto, Sumiyoshi, Osaka 558-8585, Japan
[ak] Nambu Yoichiro Institute for Theoretical and Experimental Physics, Osaka Metropolitan University, Sugimoto, Sumiyoshi, Osaka 558-8585, Japan
[al] National Institutes for Quantum and Radiation Science and Technology, 4-9-1 Anagawa, Inage, Chiba 263-8555, Japan
[am] Institute for Space-Earth Environmental Research Center for Orbital and Suborbital Research, Nagoya University, Furo, Chikusa, Nagoya 464-8601, Japan
[an] College of Science, Ibaraki University, 2-1-1 Bunkyo, Mito, Ibaraki 310-8512, Japan

Received 15 January 2024; received in revised form 19 March 2024; accepted 17 April 2024
Available online 23 April 2024

Abstract

The Calorimetric Electron Telescope, CALET, is an astroparticle physics mission installed on the International Space Station, ISS. The primary objective of the mission is studying the details of galactic cosmic-ray acceleration and propagation, and searching for the possible nearby sources of high-energy electrons and dark matter signatures. The CALET experiment measure the flux of cosmic-ray electrons (including positrons) to 20 TeV, gamma-rays to 10 TeV and nuclei to 1000 TeV. The detector is an all-calorimetric instrument with a total vertical thickness of 30 radiation lengths and fine imaging capability, optimized for the measurement of the electron and positron (all-electron) spectrum well into the TeV energy region. It consists of a charge detector (CHD) with two layers of segmented plastic scintillators for the identification of cosmic-rays via a measurement of their charge over the range $Z = 1 \sim 40$, a 3 radiation length thick tungsten-scintillating fiber imaging calorimeter (IMC) and a 27 radiation length thick lead-tungstate calorimeter (TASC). The instrument was launched on August 19, 2015 to the ISS and installed on the Japanese Experiment Module-Exposed Facility. Since the start of operation in October, 2015, CALET has been collecting scientific data without any major interruption for more than eight years. The number of triggered events over 10 GeV is nearly 1.97 billion events as of November 30, 2023. In this paper, we present the results of the CALET mission so far, including the all-electron energy spectrum, the spectra of protons and other nuclei, gamma-ray observations, as well as the characterization of on-orbit performance. Some results on the electromagnetic counterpart search for LIGO/Virgo gravitational wave events and the observations of solar modulation and gamma-ray bursts are also included.

Keywords: Galactic cosmic rays; Nearby cosmic-ray sources; Cosmic-ray acceleration; Propagation in Galaxy; International Space Station

1. Introduction

The CALorimetric Electron Telescope, CALET, is a space mission on the International Space Station, ISS (Torii and Marrocchesi, 2019). The instrument was launched on August 19, 2015 with the Japanese carrier H-IIB, delivered to the ISS by the HTV-5 Transfer Vehicle, and installed on the Japanese Experiment Module Exposed Facility (JEM-EF). The mission is managed by an international collaboration led by the Japanese Space Agency (JAXA) with the participation of the Italian Space Agency (ASI) and NASA.

The main purpose of the CALET mission is to search for nearby cosmic-ray sources and signatures of dark matter by measuring the electron spectrum (including positrons) up to 20 TeV. The detector is optimized to

precisely measure the electron flux with excellent energy resolution and high proton-rejection power. CALET is also capable of measuring the energy spectra and the relative abundances of nuclei up to the highest energies ever directly observed (approaching the PeV scale) with individual element charge resolution. In addition to the charged cosmic-rays, the observation of high energy gamma-rays from 1 GeV to 10 TeV is carried out in conjunction with the CALET Gamma-ray Burst Monitor (CGBM) which covers from the hard X-ray to the soft Gamma-ray region (7 keV – 20 MeV). CALET contributes also observations of the solar modulation of electrons and protons in the 1–10 GeV energy range, and to the detection of the MeV electrons from the radiation belt (relativistic electron precipitation: REP) for space weather.

In this paper we report the latest results of CALET including the spectra of electrons, protons and nuclei, after eight years of operations on the ISS. We also summarize the present status of other CALET measurements.

2. CALET instrument

CALET is composed of two detectors: a calorimeter and a gamma-ray burst monitor. Fig. 1 shows the CALET payload. The main detector, the calorimeter, is an all-calorimetric instrument, with a total vertical thickness equivalent to 30 radiation length (X_0) or 1.3 proton interaction lengths (λ_I), preceded by a charge identification system. Fig. 2 shows a schematic side view of the detector in which a simulated 1 TeV electron shower is overwritten. The calorimeter consists of a charge detector (CHD), a 3 radiation-length thick imaging calorimeter (IMC), and a 27 radiation-length thick total absorption calorimeter (TASC). It has a field of view of approximately 45 degrees from zenith and a geometrical factor of about 1040 cm^{2}sr for high-energy electrons.

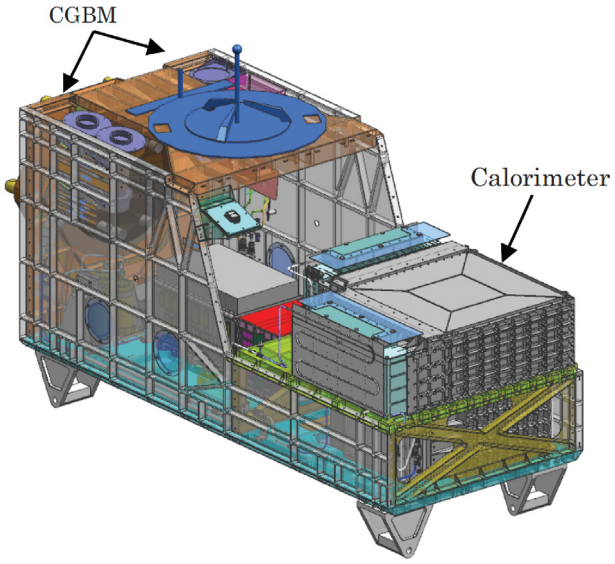

Fig. 1. Overview of CALET payload.

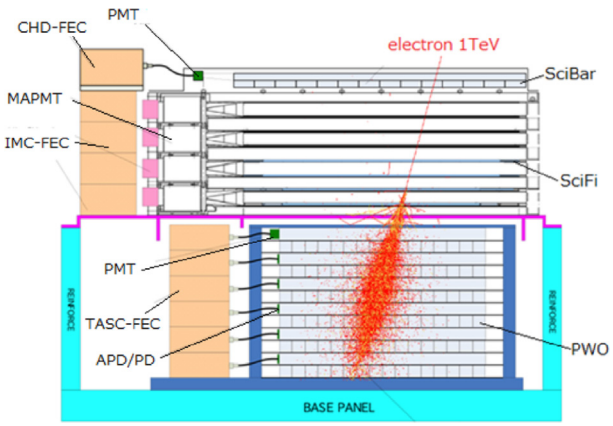

Fig. 2. Schematic view of the calorimeter with simulated 1 TeV electron shower over written.

The CHD placed at the top of the detector is designed to measure the charge of incident particles. It consists of a double layered, segmented, plastic scintillator array. Each layer comprises 14 plastic scintillator bars (SciBar), with dimensions 450 × 32 × 10 mm^3. The segmented configuration and the two layers of paddles orthogonally arranged are optimized to reduce multi-hits on each paddle caused by backscattered particles produced in the detectors. The scintillation light generated in each paddle is collected and read out by one photomultiplier tube (PMT), and the resulting output is sent to a front end circuit (FEC). The CHD and related front-end electronics are designed to provide particle identification over a large dynamic range for charges from $Z = 1$ to 40 or more. The charge measurement performance was tested by the beam test at GSI (Marrocchesi et al., 2011) and at CERN-SPS (Akaike et al., 2015), and the charge resolution is 0.15 e for carbon and 0.3 e for iron.

The IMC is a sampling calorimeter of 1 mm square cross section scintillating fibers (SciFi) and tungsten plates to measure the initial shower development and arrival direction. It contains a total of 16 detection layers, arranged in 8 $X - Y$ pairs, with each layer segmented into 448 parallel SciFis, which are individually read out by 64-channel multi-anode PMTs (MAPMTs). Each of the first 5 tungsten plates is 0.2 X_0 thick while the last 2 layers are 1.0 X_0. Above several tens of GeV, the angular resolution for electrons is 0.16°, while for gamma-rays 0.24°. The dE/dx measurements of IMC layers provide a charge resolution of 0.20e for carbon.

The TASC is designed to measure the total energy of the incident particle and discriminate electromagnetic from hadronic showers. It consists of 12 layers, with 16 lead tungstate (PWO) logs, each 326 × 19 × 20 mm^3. Layers are arranged alternatively in X and Y to provide a 3D reconstruction of the shower images. Each PWO log of the top layer is read out by a PMT to generate a trigger signal, and the logs of the other layers are read out by hybrid packages of silicon avalanche photodiode (APD) and silicon photodiode(PD). Two shaping amplifiers with different

gains for each APD and PD (PMT) are used to achieve a dynamic range of 10^6 (10^4), which allows each log to measure signals from 0.5 MIPs (Minimum Ionizing Particles) to 10^6 MIPs corresponding to the energy deposit by a proton-induced by 1000 TeV shower. Combining these detectors, the CALET instrument achieves an energy resolution of 2% for electrons above 20 GeV, and a proton rejection power of 10^5. The instrument is described in more detail elsewhere (Adriani et al., 2017).

3. Performance and operation

Very stable observations have continued by cooperation of JAXA Ground Support Equipment (JAXA-GSE) and the Waseda CALET Operations Center (WCOC) (Asaoka et al., 2018). The observation mode on orbit is controlled by a regular schedule of command sequences. A continuously active high-energy trigger (HE) mode ensures maximum exposure to high-energy electrons and other high-energy shower events with $E > 10$ GeV. The other modes include a low-energy trigger at the highest geomagnetic latitude, a low-energy gamma-ray trigger at low geomagnetic latitudes, and an ultra-heavy trigger mode that is almost continuously active (except for high latitude during the calibration mode). In addition, the calibration mode to detect minimum ionizing particles is active for three hours per day. The total observation time was 2971 days as of November 30, 2023. The live-time fraction was 86% for this period. More than 1.97 billion events were observed in HE trigger mode.

To achieve an excellent energy measurement, the calibration errors must be carefully evaluated and considered in the energy estimation. Our energy calibration includes an evaluation of conversion factors between ADC units and energy deposits, confirming linearity over each of the gain ranges (TASC has four gain ranges for each channel), as well as a seamless transition between adjacent gain ranges. Temporal gain variations that occur during long-term observations are also corrected in the calibration. We have estimated the errors at each calibration step, such as the correction of position and temperature dependence, linear fit procedure of each gain range, gain ratio measurements, and slope extrapolation, as well as the errors of MIP calibration inferred from the degree of consistency between energy deposit peaks of non-interacting protons and helium. The errors are included in the estimation of the energy resolution. This results in a very high resolution of 2% or better above 20 GeV (Asaoka et al., 2017). The TASC energy deposit spectrum based on all triggered events through the end of November 2023 is shown in Fig. 3. The first (~2 GeV) and second (~5 GeV) bumps are due to low-and high-energy triggered events, respectively, whereas the high-energy tail is due to the power-law nature of the cosmic-ray spectrum. The spectrum spans more than six orders of magnitude in energy, from below 1 GeV to above 1 PeV. This clearly demonstrates the reliability of CALET energy measurements over a very wide dynamic range.

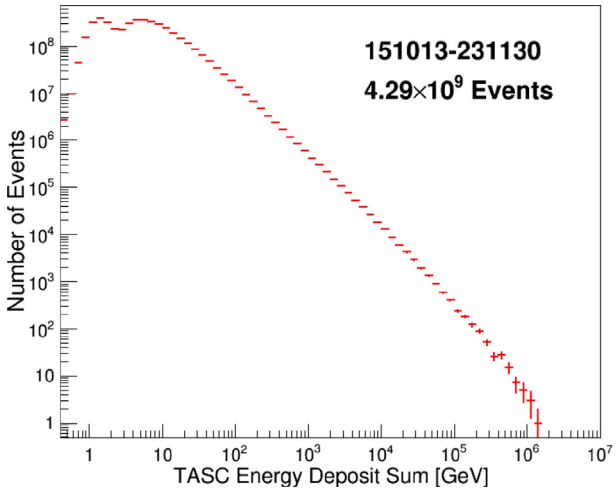

Fig. 3. Energy distribution of all triggered events as a function of TASC energy.

Monte Carlo (MC) simulations, reproducing the detailed detector configuration, physics process, as well as detector signals, are based on the EPICS simulation package (Kasahara, 1995) and employ the hadronic interaction model DPMJET-III (Roesler et al., 2001); it was tuned and tested with accelerator beam test data. An independent analysis based on FLUKA (Ferrari et al., 2005; Böhlen et al., 2014) and Geant4 (Agostinelli et al., 2003) is also performed to assess the systematic uncertainties.

4. Results

4.1. Electron and positron spectrum

The CALET detector is optimized for the precise measurement of the all-electron spectrum from 10 GeV to 20 TeV with a field of view of 45 degrees from the zenith and a geometrical factor of 1040 cm^2sr at high energies. The 30 X_0 thick calorimeter allows for a full containment of electron showers even at the TeV scale, with an excellent energy resolution (< 2% above 20 GeV), while proton showers with equivalent energy deposit undergo a larger energy leakage from the bottom layers of the TASC. These features are exploited to separate electrons from protons, leveraging on the capability of the TASC and IMC to image the longitudinal and lateral profiles of electromagnetic and hadronic cascades. Two methods were applied to identify electrons and to study systematic uncertainties in the electron identification; a simple two-parameter cut and a multivariate analysis based on boosted decision trees (BDTs). In the final electron sample, the residual contamination of protons is 5% up to 1 TeV, and less than 10% in the 1–7.5 TeV region, while keeping a constant high efficiency of 70% for electrons including the efficiency of the

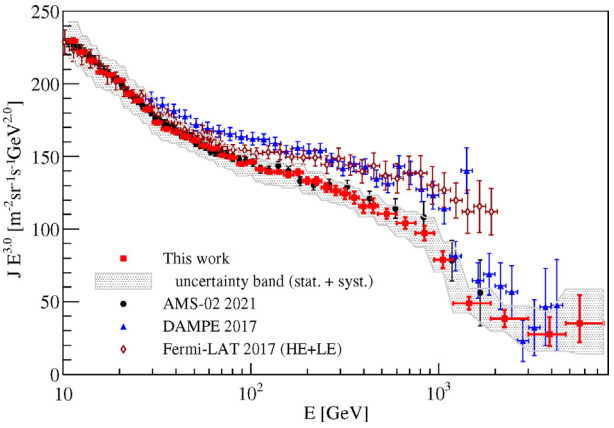

Fig. 4. All-electron spectrum observed with CALET from 10.6 GeV to 7.5 TeV, where the gray band indicates the quadratic sum of statistical and systematic errors (Adriani et al., 2023a). Also plotted are other direct measurement in space (Abdollahi et al., 2017; Ambrosi et al., 2017; ?).

pre-selection such as an off-line trigger confirmation, a track quality cut and a charge selection.

The latest results of the electron + positron (all-electron) spectrum with CALET are shown in Fig. 4, based on 2637 days of flight data collected with the HE trigger (Adriani et al., 2023a). The spectrum integrates 7.02 million electron (+positron) events above 10.6 GeV to 7.5 TeV. The error bars along the horizontal and vertical axes are representative of the bin width and statistical errors, respectively. The gray band bounds the quadrature sum of statistical and systematic errors.

Systematic uncertainties include the absolute normalization error as well as energy dependent errors stemming from BDT stability, trigger efficiency in the low-energy region, tracking performance, dependence on charge and electron identification methods, and MC model dependence. Conservatively, all of them are included in the total error estimated in Fig. 4. The absolute energy scale was calibrated and shifted by + 3.5% as a result of studies of the geomagnetic cutoff energy (Adriani et al., 2017). The systematic uncertainties are described in more detail in (Adriani et al., 2023a).

Comparing with the other space experiments (Fermi-LAT (Abdollahi et al., 2017), AMS-02 (Aguilar et al., 2021a) and DAMPE (Ambrosi et al., 2017)), the CALET spectrum shows a good agreement with AMS-02 data up to 2 TeV, where both experiments have a good electron identification capability, albeit using different detection techniques. In the energy region from 30 to 300 GeV, the fitted power-law spectrum index, -3.14 ± 0.02, is roughly consistent with the values quoted by other experiments within the errors. The CALET spectrum, however, appears to be softer compared to Fermi-LAT and DAMPE, and the flux observed by CALET is lower than these two experiments, starting near 60 GeV and extending to near 1 TeV, possibly indicating the presence of unknown systematic errors.

The electron energy spectrum above 1 TeV is expected to show a break due to the radiative cooling process with

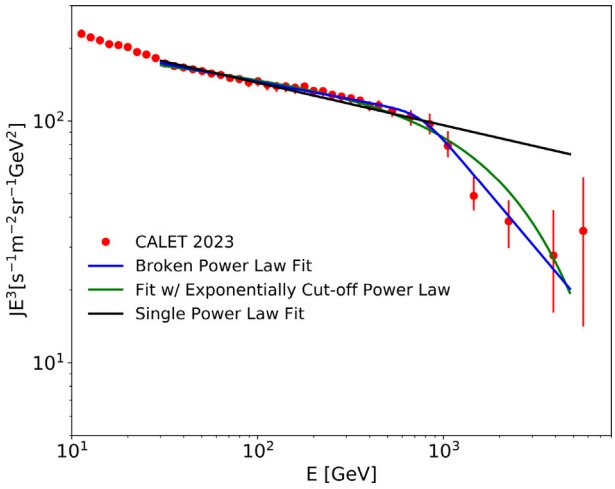

Fig. 5. All-electron spectrum measured by CALET from 10.6 GeV to 7.5 TeV, and the fitted results in the energy range from 30 GeV to 4.8 TeV, with a broken power law, an exponentially cutoff power law and a single power law(Adriani et al., 2023a). The error bars represent statistical and systematic uncertainties except normalization.

an energy loss rate proportional to E^2. As a result, only nearby (<1 kpc) and young ($< 10^5$ years) sources can contribute to the flux above 1 TeV if the sources are supernova remnants (SNRs) as it is commonly believed as mentioned in Nishimura et al. (1980); Kobayashi et al. (2004).

The expected flux suppression above 1 TeV is clearly seen by CALET, which is consistent with DAMPE within the errors. As presented in Fig. 5, the spectrum is fitted in the energy range from 30 GeV to 4.8 TeV with a broken power law and an exponentially cutoff power law. The significance of the both fits is more than 6.5σ compared to a single-power law fit with an index of -3.18 ± 0.01.

Combining the CALET all-electron spectrum and the positron measurements up to 1 TeV by AMS-02, we attempt a consistent interpretation of both spectra based on the contributions from pulsars and nearby SNR

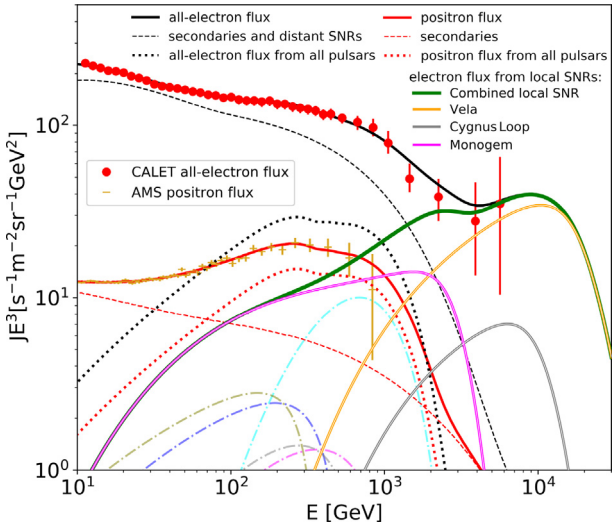

Fig. 6. Possible spectral fit over the whole region of CALET observations, including pulsars and nearby SNR sources as individual sources, with the Vela SNR dominating in the TeV region(Adriani et al., 2023a).

sources. We have incorporated the measured AMS-02 positron flux (Aguilar et al., 2021a), source and propagation parameters suggested in Motz et al. (2021), and the results from the numerical propagation code DRAGON (Evoli et al., 2017; Fornieri et al., 2020) to construct a possible model that fits the CALET all-electron measurements. Fig. 6 shows an example of prediction by the model fitted consistently with the CALET results and the AMS-02 positron results. The positron flux of AMS-02 is fitted with contributions from secondaries (red dashed line) + several pulsars (red dotted line), while the all-electron flux is fitted with the sum of electron and positron flux from the pulsars (black dotted line), in addition to secondaries + distant SNRs (black dashed line) with a cutoff at 1 TeV. Above 1 TeV, we include the nearby SNRs, Vela (orange solid line), Cygnus Loop (gray solid line), and Monogem (magenta solid line) as the dominant sources (Kobayashi et al., 2004), with their combined contribution (green line). The best fit yields an energy output of 0.8×10^{48} erg in electron cosmic rays above 1 GeV for each nearby SNR.

4.2. Proton and helium spectra

The latest proton spectrum with CALET is shown in Fig. 7, based on 2757 days of operation with the HE trigger and 365.4 h of live time with the LE trigger, respectively. It is an update of the published CALET proton spectrum (Adriani et al., 2022a) with an increase of the statistics by 21%, using the same analysis method, and the energy range is from 50 GeV to 60 TeV (Kobayashi et al., 2023). In the same figure the CALET flux is compared with AMS-02 (Aguilar et al., 2015a; Aguilar et al., 2021a), CREAM-III (Yoon et al., 2017), and DAMPE (An et al., 2019). In the energy range below 1 TeV, the CALET proton spectrum is well consistent with AMS-02 and DAMPE. On the contrary, the spectrum from 1 TeV to 60 TeV is systematically lower than that of DAMPE by ~10%, though the difference is within the uncertainties. We confirm the presence of a spectral hardening around 500 GeV as reported in Adriani et al. (2022a). We also observe a spectral softening around 10 TeV. In order to quantify the spectral hardening and softening, we fit the proton spectrum using a double broken power law (DBPL) function defined as follows,

$$\Phi(E) = C\left(\frac{E}{1\mathrm{GeV}}\right)^{\gamma}\left[1+\left(\frac{E}{E_0}\right)^{S}\right]^{\frac{\Delta\gamma}{S}}\left[1+\left(\frac{E}{E_1}\right)^{S_1}\right]^{\frac{\Delta\gamma_1}{S_1}}, \quad (1)$$

where C is a normalization factor, γ is the spectral index, E_0 is a characteristic energy of the region where a gradual spectral hardening is observed, $\Delta\gamma$ the spectral variation due to the spectral hardening, E_1 a characteristic energy of the transition to the region of spectral softening, $\Delta\gamma_1$ the spectral index variation observed above E_1. Two independent smoothness parameters S and S_1 are introduced in the energy intervals where spectral hardening and softening occur, respectively. In Fig. 8, the black filled circles show the data with statistical errors and the red line shows the best fitted function for $\Phi\prime(E) = E^{2.7} \times \Phi(E)$. The chi-square is 6.0 with 20 degrees of freedom.

The energy spectrum of helium measured with CALET in 2392 days of operation is shown in Fig. 9 covering an interval of kinetic energy per particle from 40 GeV to 250 TeV(Adriani et al., 2023b), compared with previous observations from space-based(Aguilar et al., 2015b; Aguilar et al., 2021a; Alemanno et al., 2021) and balloon-borne (Yoon et al., 2011) experiments. The spectrum is in good agreement with the very accurate measurements by AMS-02 in the lower energy region below a few TeV, as well as with the measurements from calorimetric instruments in the higher energy region, in particular with the recent measurement of DAMPE. In Fig. 10, a fit of the helium spectrum is performed using a DBPL function in the energy range from 60 GeV to 250 TeV. A progressive hardening

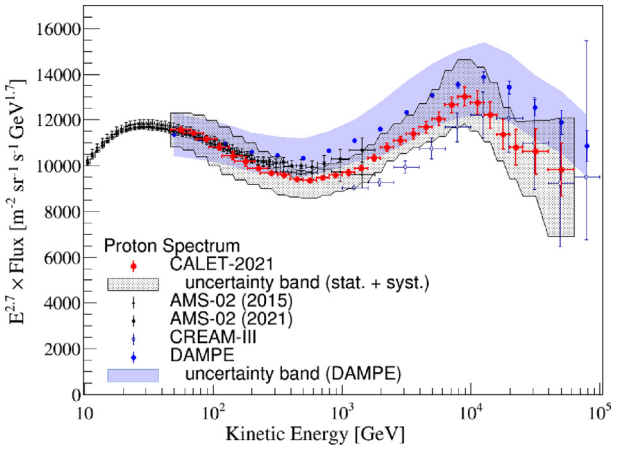

Fig. 7. Proton spectrum measured by CALET from 50 GeV to 60 TeV (Kobayashi et al., 2023) compared with other experiments (AMS-02 (Aguilar et al., 2015a; Aguilar et al., 2021a), CREAM-III (Yoon et al., 2017), DAMPE (An et al., 2019)). The hatched band shows the total uncertainty for CALET as the quadratic sum of the various uncertainties. The dark blue colored band shows the total uncertainty for DAMPE. (For interpretation of the references to colour in this figure legend, the reader is referred to the web version of this article.)

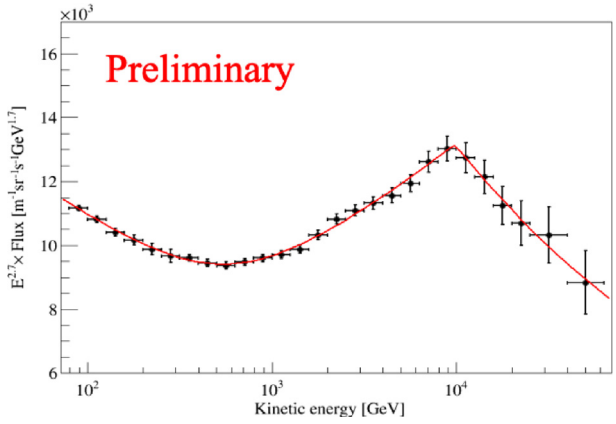

Fig. 8. CALET proton spectrum fitted by a DBPL function (Eq. 1), and the fit parameters are shown in Table 1. The horizontal error bars are representative of the bin width.

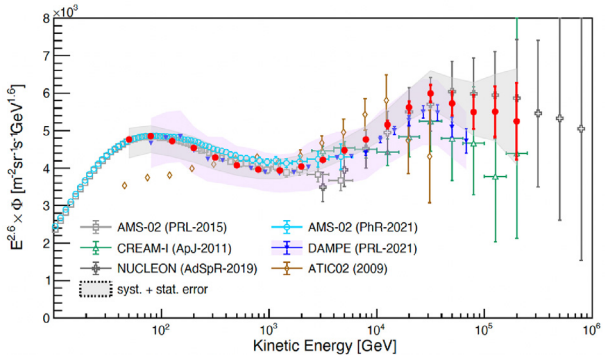

Fig. 9. Helium spectrum measured by CALET from 40 GeV to 250 TeV (Adriani et al., 2023b), compared with previous direct measurements (Yoon et al., 2011; Aguilar et al., 2015b; Aguilar et al., 2021a; Alemanno et al., 2021). The error bars represent only the statistical error; the gray band represents the quadratic sum of statistical and systematic errors.

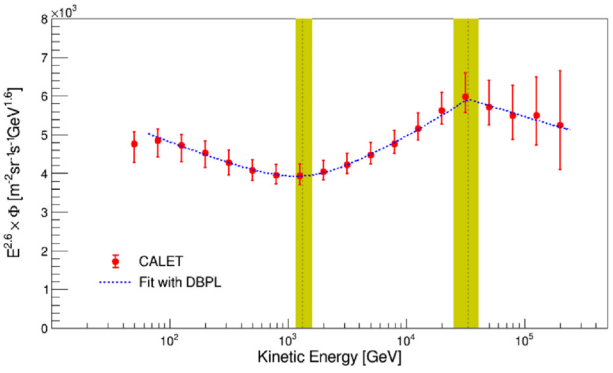

Fig. 10. CALET helium spectrum with a DBPL function (Eq. 1), and the fit parameters are shown in Table 1. The result is consistent with the recent measurement by Alemanno et al. (2021) within the errors. Both statistical and systematic uncertainties are taken into account.

Table 1
Best fit parameters with DBPL function for proton and helium spectra.

	Proton	Helium
γ	-2.843 ± 0.005	$-2.703^{+0.005}_{-0.006}$
E_0 (GeV)	553^{+44}_{-38}	1319^{+113}_{-93}
$\Delta\gamma$	0.29 ± 0.01	$0.25\pm^{0.02}_{-0.01}$
S	2.1 ± 0.4	$2.7^{+0.6}_{-0.5}$
E_1 (TeV)	$9.8^{+3.2}_{-2.1}$	$33.2^{+9.8}_{-6.2}$
$\Delta\gamma_1$	$-0.39^{+15}_{-0.18}$	$-0.22^{+0.07}_{-0.10}$
S_1	~ 90	30

from a few hundred GeV to a few tens TeV and the onset of a flux softening above a few tens of TeV are observed as indicated by the yellow bands. The best fit parameters (with statistical errors only) are summarized in Table 1 to be compared with the proton results.

Differences between the proton and helium spectra can contribute important constraints on acceleration models. Fig. 11 shows the CALET proton spectrum (Adriani et al., 2022a) and the helium spectrum (Adriani et al., 2023b) as a function of rigidity. The ^{3}He contribution to the flux is taken into account assuming the same ^{3}He/^{4}He ratio as measured by AMS-02 (Aguilar et al., 2019) and

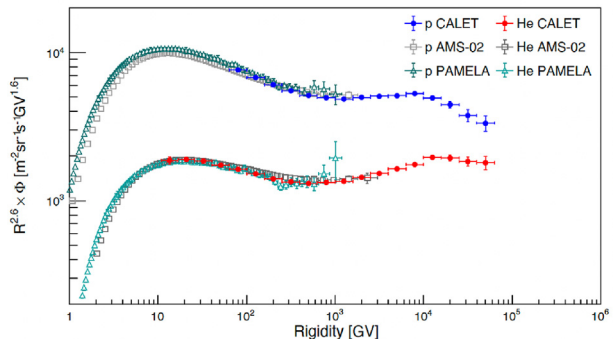

Fig. 11. Proton and helium spectra with CALET as a function of rigidity (Adriani et al., 2022a; Adriani et al., 2023b), together with previous observations(Adriani et al., 2011; Aguilar et al., 2021a). Only the statistical errors are shown.

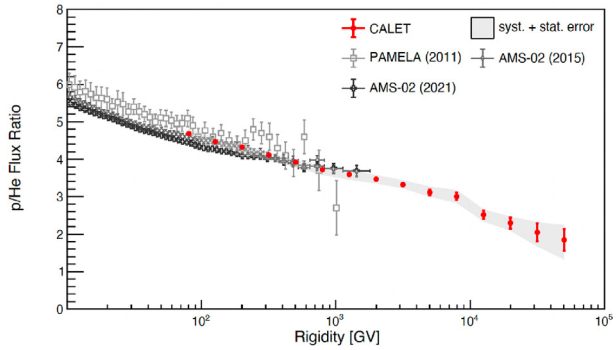

Fig. 12. p/He ratio as measured by CALET as a function of rigidity (Adriani et al., 2023b). The red vertical bars represent statistical error only while the gray band represents the quadratic sum of statistical and systematic errors. Previous measurements (Adriani et al., 2011; Aguilar et al., 2015b; Aguilar et al., 2021a) are also shown.

extrapolating the ratio to higher energies with use of a single power-law fit. Measurements from other experiments (Adriani et al., 2011; Aguilar et al., 2021a) are included in these plots. The CALET results are found to be in agreement with measurements from the magnetic spectrometers up to their maximum detectable rigidity (~2 TV). The p/He flux ratio measured by CALET is presented in Fig. 12 as a function of rigidity(Adriani et al., 2023b) with other experimental data(Adriani et al., 2011; Aguilar et al., 2021a).

4.3. Boron, Carbon and oxygen spectra and their ratios

The boron, carbon, and oxygen spectra from 8.4 GeV/n to 3.8 TeV/n are shown in Fig. 13 based on 2554 days of CALET operation (Maestro et al., 2023), with higher statistics than published in Adriani et al. (2020); Adriani et al. (2022d). The analysis method is the same as described in Adriani et al. (2022d), and the latest results are in complete agreement with our published data. The total background contamination in the boron sample is 1% for $E_{\mathrm{TASC}} < 10^2$ GeV and grows logarithmically with E_{TASC} above 10^2 GeV, approaching 7% at 1.5 TeV. The background contamination is less than 1% for carbon and oxygen. The isotopic composition of boron is assumed to be

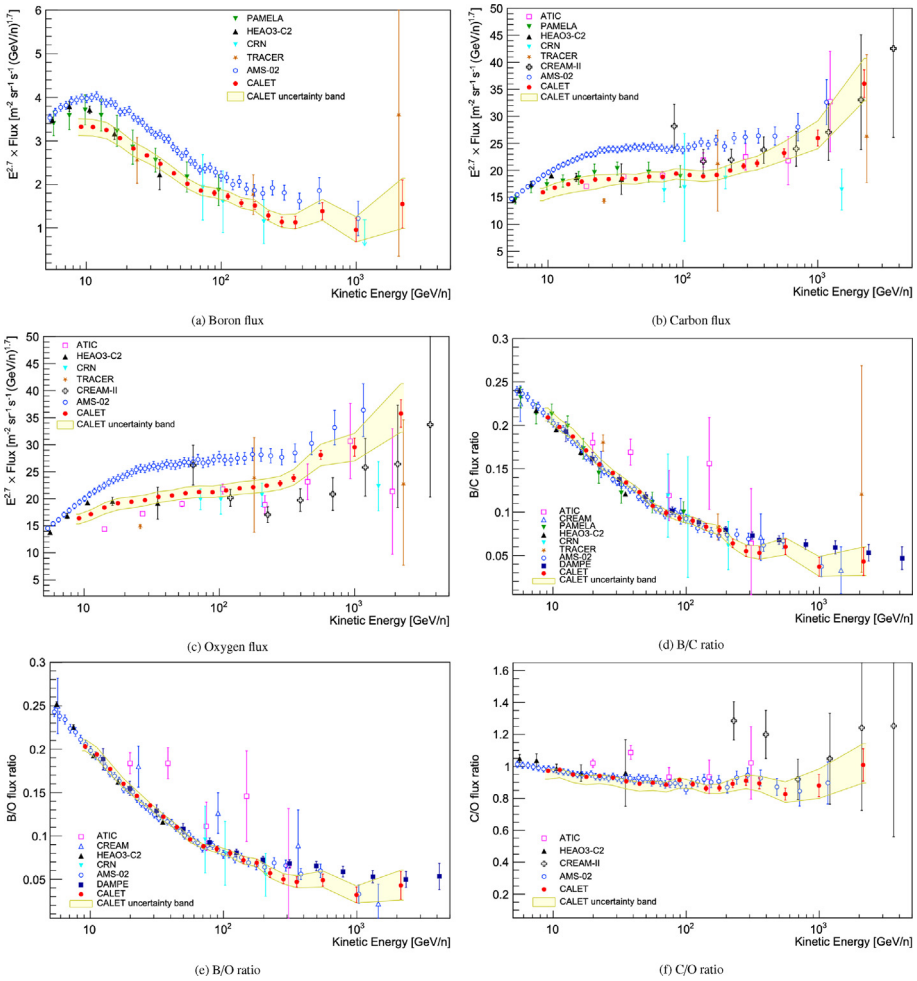

Fig. 13. CALET (a) boron, (b) carbon and (c) oxygen fluxes multiplied by $E^{2.7}$, and ratio of (d) boron to carbon, (e) boron to oxygen, and (f) carbon to oxygen from 10 GeV/n to 3.8 TeV/n as a function of kinetic energy per nucleon(Maestro et al., 2023). Error bars of CALET data (red) represent the statistical uncertainty only, while the yellow band indicates the quadratic sum of statistical and systematic errors. Also plotted are other direct measurements (Engelmann et al., 1990; Swordy et al., 1990; Ahn et al., 2008; Obermeier et al., 2012; Adriani et al., 2014; Aguilar et al., 2021a; Alemanno et al., 2022; Panov et al., 2009; Ahn et al., 2009).

$^{11}B/(^{10}B+^{11}B) = 0.7$ for all energies. Different values of the isotope ratio (0.6 and 0.8) make only a 2% difference in the boron spectrum. The main contribution of the systematic errors comes from the different MC simulations (EPICS vs. Geant4) used in the analysis, which produce similar selection efficiencies but energy response differing significantly in the low- and high-energy regions. The resulting fluxes for B (C, O) show discrepancies not exceeding 6% (10%, 4.5%) below 20 GeV/n and 12% (10%, 12%) above 300 GeV/n, respectively, and they are included in the systematic uncertainties. In Fig. 13, the energy spectra of B, C and O with CALET are shown and compared with earlier results from space-borne (Adriani et al., 2014; Engelmann et al., 1990; Swordy et al., 1990; Aguilar et al., 2021a) and balloon-borne (Ahn et al., 2008; Obermeier et al., 2012; Panov et al., 2009) experiments. These spectra of CALET are consistent with PAMELA (Adriani et al., 2014) and most of the earlier experiments but the absolute normalization is in tension with AMS-02. We notice that CALET and AMS-02(Aguilar et al., 2017) spectra have very similar shapes but they differ in the absolute normalization, which is lower for CALET by about 27%. The B/C, B/O, and C/O ratios are, however, consistent with the ones measured by AMS-02 as shown in Fig. 13.

Fig. 14 shows the fits to CALET carbon and oxygen data with a double power-law (DPL) function:

$$\Phi(E) = \begin{cases} C\left(\frac{E}{\mathrm{GeV}}\right)^{\gamma} & E \leqq E_0 \\ C\left(\frac{E}{\mathrm{GeV}}\right)^{\gamma}\left(\frac{E}{E_0}\right)^{\Delta\gamma} & E > E_0 \end{cases} \quad (2)$$

where C is a normalization factor, γ is the spectral index, and $\Delta\gamma$ is the spectral index change above the transition energy E_0. A single power-law (SPL) function, fitted to the data in the energy range from 25 GeV/n to 200 GeV/n and extrapolated above 200 GeV/n, is also shown for comparison.

The simultaneous DPL fit to the C and O spectra in the energy range from 25 to 3800 GeV/n yields $\gamma_{CO} = -2.66 \pm 0.02, \Delta\gamma_{CO} = 0.19 \pm 0.04$ and $E_0 = 260 \pm 50$

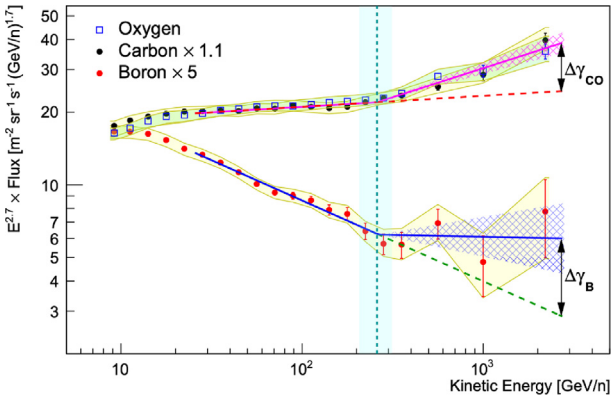

Fig. 14. CALET B (red dots), C (black dots) and O (blue open squares) energy spectra are fitted with DPL functions (magenta line for the fit to the combined C and O data, blue line for B)(Maestro et al., 2023). The B spectrum is multiplied by a factor 5 to overlap the low-energy region of the C and O spectra. Error bars represent the statistical uncertainty only, while the yellow (green for O) bands indicate the quadratic sum of statistical and systematic errors. The dashed lines represent the extrapolation of a SPL function fitted to data in the energy range from 25 to 200 GeV/n. The magenta (blue) cross-shaded area shows the $\pm1\sigma$ error interval of $\delta\gamma$ from the fit to C and O (B) data. The value of the transition energy E_0 is represented by the vertical cyan dashed line, while the cyan band shows its $\pm1\sigma$ error interval. (For interpretation of the references to colour in this figure legend, the reader is referred to the web version of this article.)

GeV/n confirming our first results reported in Adriani et al. (2020). Fitting the B flux with fixed E_0 yields $\gamma_B = -3.03 \pm 0.03, \Delta\gamma_B = 0.32 \pm 0.14$ with χ^2/d.o.f.= 5.2/11. The energy spectra are clearly different as expected for primary and secondary CR, and the fit results seem to indicate, albeit with low statistical significance, that the flux hardens more for B than for C and O above 200 GeV/n. A similar indication also comes from the simultaneous fit to the B/C and B/O flux ratios as shown in Fig.15. Fitting the SPL functions to B/C and B/O ratios in the energy range from 25 GeV/n to 3800 GeV/n yields a mean spectral index $\Gamma = 0.376 \pm 0.014$ (χ^2/d.o.f.= 19/27). However, a DPL function provides a better fit suggesting a trend of the data towards a flattening of the B/C and B/O ratios at high energy, with a spectral index change $\Delta\Gamma = -0.22 \pm 0.10$ (χ^2/d.o.f.= 15/26) above E_0, which is left as a fixed parameter in the fit. This result is consistent with that of AMS-02 (Aguilar et al., 2021a), and supports the hypothesis that secondary B exhibits a stronger hardening than primaries C and O, although no definitive conclusion can be drawn due to the large uncertainty in $\Delta\Gamma$ given by our present statistics. For the Leaky Box Model fit (Obermeier et al., 2012), the fit with a residual material around SNR of ~ 1 g/cm^2 gives a better fit than zero material as shown in Fig. 15 (Maestro et al., 2023).

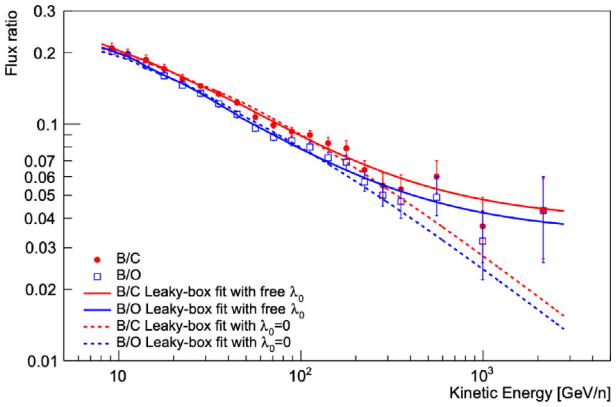

Fig. 15. Simultaneous fit of the CALET B/C and B/O flux ratios with a leaky-box model leaving the λ_0 parameter free to vary (solid line) or fixing it at zero (dashed line), respectively(Maestro et al., 2023). The error bars are the quadratic sum of the statistical and systematic uncertainties.

4.4. Iron and Nickel spectra

Fig. 16a shows the preliminary iron spectrum in kinetic energy per nucleon in the energy range from 10 GeV/n to 1000 GeV/n based on 2618 days of operation (Stolzi

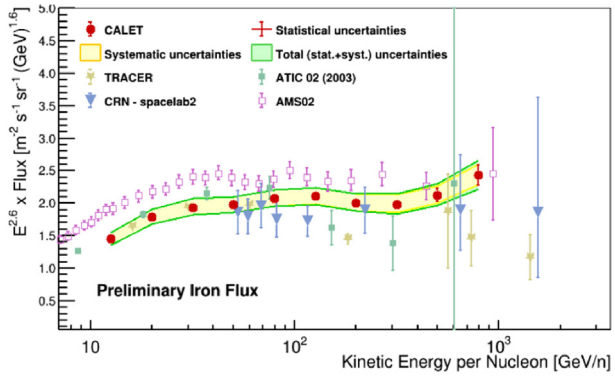

(a) Iron flux

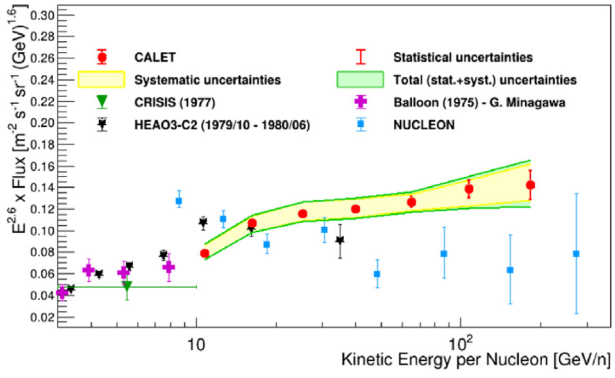

(b) Nickel flux

Fig. 16. CALET (a) iron and (b) nickel) flux multiplied by $E^{2.6}$ as a function of kinetic energy per nucleon(Stolzi et al., 2023). Error bars of the CALET data (red) represent the statistical uncertainty only, the yellow band indicates the quadrature sum of systematic errors, while the green band indicates the quadrature sum of statistical and systematic errors. Also plotted are other direct measurements (Grebenyuk et al., 2018; Engelmann et al., 1990; Minagawa, 1981; Young et al., 1981; Panov et al., 2009; Ave et al., 2008; Mueller et al., 1991; Aguilar et al., 2021bs). (For interpretation of the references to colour in this figure legend, the reader is referred to the web version of this article.)

et al., 2023). The statistics is increased by a factor of 2 compared to the previous publication (Adriani et al., 2021). We have found that the iron spectrum obtained by EPICS is consistent with the spectrum by Geant4 above 100 GeV/*n*, while differing in normalization in the low energy region by about 10%. This can be attributed to the response matrices, which differ significantly in the low-energy region. Fig. 16b shows the nickel spectrum in kinetic energy per nucleon in the energy range from 8.8 GeV/*n* to 240 GeV/*n* based on the same period as the case of iron (Stolzi et al., 2023). Here, The latest data is consistent with our previous publication (Adriani et al., 2022b), whilethe statistics are increased by a factor of 1.3.

Fig. 17a shows the fit to the Fe flux with a DPL function (Eq. 2). A SPL function is also shown for comparison. The DPL fit, performed from 50 GeV/*n* to 1 TeV/*n*, gives a $\gamma = -2.60 \pm 0.01$ (stat) ± 0.08 (sys), $\Delta\gamma = 0.29 \pm 0.27$ and $E_0 = (428 \pm 314)$ GeV/*n* with $\chi^2/d.o.f. = 2.7/5$. The significance of the fit with the DPL in the studied energy range is not sufficient to exclude the possibility of a single power law. Fig. 17b shows the fit to the Ni flux with a SPL function performed from 20 GeV/*n* to 240 GeV/*n*. The fit result gives $\gamma = -2.49 \pm 0.03$ (stat) ± 0.07 (sys) with $\chi^2/d.o.f. = 0.1/3$. This result shows that the Ni flux, in the fit energy range, is compatible within the errors with a single power law.

4.5. Ultra heavy cosmic rays

The measurement of ultra heavy galactic cosmic rays (UHGCR), ^{30}Zn and higher charge elements, provides insight into the origins of cosmic rays. CALET's measurements of cosmic-ray abundances up to $Z \leq 44$ charge range provide complementary measurements and a check of the cross calibrations of other instruments. As described in Asaoka et al. (2018), CALET has a trigger mode to measure ultra heavy (UH) nuclei called UH trigger, which requires a coincidence of signals of CHD and upper 4 IMC layers. This corresponds to an acceptance angle of 75°, which gives an enhanced geometry factor of 4400 cm^2-sr. In this trigger, one needs to use the minimum geomagnetic cutoff as a proxy for energy. Here we explore usage of a subset of UH trigger data that requires particles to pass through part of the TASC (~65 million events) (Zober et al., 2023). In addition to the standard calibration using the minimum ionizing particles of protons and helium nuclei (Asaoka et al., 2017), heavy nuclei such as iron and silicon, which have large dE/dx, are utilized to achieve a ~0.5% signal resolution for UH analysis. The UH event candidates are identified by requireing the deposit energy to be above 1.53 MIP and ensuring charge consistency between CHD-X and CHD-Y within 0.4%. Fig. 18 shows the charge distribution for the data set obtained during 7.5 years of operation with gaussian fits.

After performing a careful fitting, we are able to plot the relative abundances in Fig. 19, in which the results of previous experiments (Binns et al., 2022; Walsh et al., 2022; Zober, 2023) are compared. The older analysis method shown in Zober et al. (2021) that uses the UH trigger in conjunction with a geomagnetic cutoff is also shown for the comparison. In these plots, we can see good consistency between ACE measurements and CALET. We note that there are some minor differences from SuperTIGER, but these may be caused by problems with the atmospheric corrections.

4.6. Gamma-rays

High-energy gamma-rays. The performance of CALET gamma-ray sensitivity, analysis methods, and initial results for steady sources are descrived in Cannady et al. (2018). CALET has a sensitivity for gamma-rays above 1 GeV with the energy resolution of 3% and the angular resolution of 0.4° at 10 GeV. Access to energies below 10 GeV is allowed by a dedicated low-energy gamma trigger (LE-γ) which is active only at low geomagnetic latitude. The highest gamma-ray efficiency is achieved around 10 GeV with an efficiency of 50% relative to a geometrical factor of about 400 cm^{2}sr, by applying event selections. In previous analysis, we simply rejected events coming from the field-of-view affected by moving structures such as solar panels and robotic arms (Cannady et al., 2018). We have developed moving filter algorithms to reject time-varying portions of our field-of-view by taking account of moving

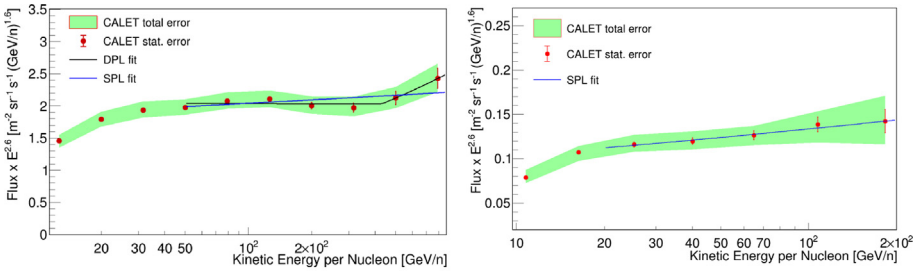

(a) Fit to the iron spectrum in the energy range from 50 GeV/*n* to 1 TeV/*n*.

(b) Fit to the nickel spectrum in the energy range from 20 GeV/*n* to 240 GeV/*n*.

Fig. 17. (a) Fit of the CALET iron energy spectrum to an SPL function (blue line) and to an DPL function (black line) in the energy range 50 GeV/*n* to 1 TeV/*n*. (b) Fit of the CALET nickel energy spectrum to an SPL function (blue line) in the energy range from 20 GeV/*n* to 240 GeV/*n*(Stolzi et al., 2023). The fluxes are multiplied by $E^{2.6}$ where E is the kinetic energy per nucleon. The error bars are representative of statistical errors only. (For interpretation of the references to colour in this figure legend, the reader is referred to the web version of this article.)

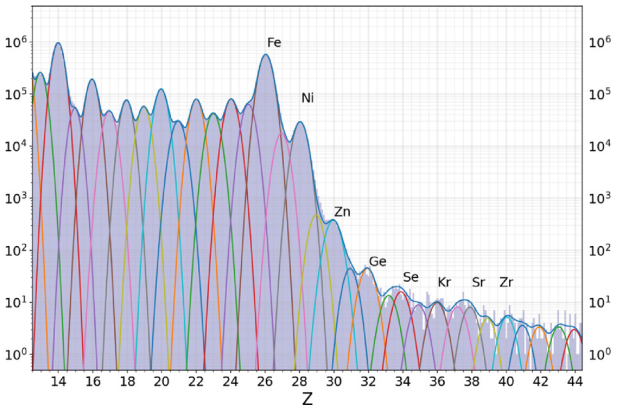

Fig. 18. The multigaussian fit for the TASC UH abundances. The number of events within the full fit is roughly identical to the number in the histogram (<1% difference between fit and histogram in the UH region).

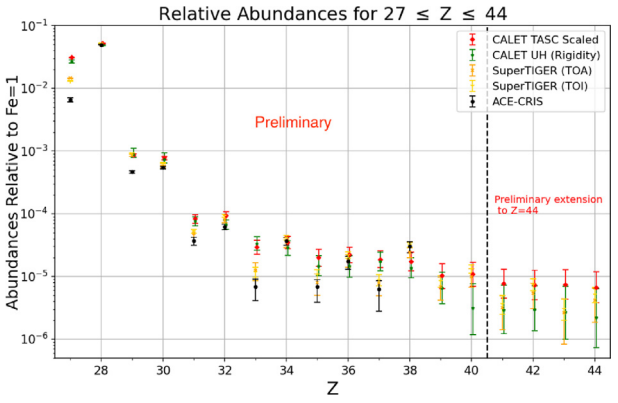

Fig. 19. CALET UH abundances for $Z > 26$(Zober et al., 2023) compared to the abundances from ACE-CRIS (Binns et al., 2022) and both SuperTIGER top of instrument (Walsh et al., 2022) and top of atmosphere (Zober, 2023).

structures, whose operational data are supplied by JAXA, operating the 'Kibo' module, in order to maximize our exposure for cosmic gamma-rays. As a result of the improved structure cut, the exposure which can be used for gamma-ray analysis is significantly increased. In the LE-γ trigger mode, the fraction of survival after the cut increased from ~60% to >90% around the peak region of the exposure map. Fig. 20 shows the skymap of gamma-ray intensities for LE-γ triggers (> 1 GeV) using data between November 2015 to December 2022 (Mori et al., 2023). Note that the exposures, superimposed as contours, are not uniform over the celestial coordinates because of inclination angle (51.6°) of the ISS orbit and our triggering schemes. One can see that the skymap matches nicely with that shown by Fermi-LAT, considering the non-uniform exposures. We can easily identify 23 bright point sources in the skymap, but the significance of the detection of each source is still under evaluation.

Without removing point sources, the Galactic plane (diffuse plus discrete sources) spectra ($|l| < 80°$ & $|b| < 8°$) are obtained in 1–100 GeV by LE-γ trigger as shown in Fig. 21. A good match is seen with the Fermi-LAT results for the Galactic plane spectrum, but with some overestimates below ~10 GeV in the off-plane spectrum ($|b| > 10°$).

CALET Gamma-ray burst monitor. The CALET gamma-ray burst monitor (CGBM), designed to observe prompt emissions of gamma-ray bursts (GRBs) in the hard *X*-ray (7–1000 keV) and soft gamma-ray (40 keV–20 MeV) band, has been providing all-sky monitoring, with 60% duty cycle and without any problems, since October 2015. The gamma-ray bursts are monitored also by the calorimeter, whose threshold is decreased to 1 GeV whenever a trigger signal is produced by the CGBM. CALET covers the energies from 7 keV to 10 TeV. The performance and analsyis procedure of CGBM are described in Adriani et al. (2022c). Fig. 22 presents the time duration distribution of GRBs observed by CGBM/SGM. As of the end of June 2023, the CGBM has detected 327 GRBs, including 31 short GRBs by classifying GRBs with the intersection of two logarithmic normal distributions (Kawakubo et al., 2021).

CALET has actively participated in the follow-up campaign for the search of electromagnetic counterparts of the gravitational wave events observed by LIGO/Virgo. Although no candidates have been detected, upper limits

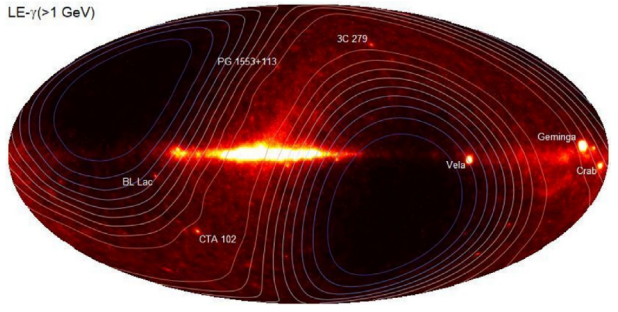

Fig. 20. Sky map by LE-γ triggers ($E > 1$ GeV) showing gamma-ray intensities observed in galactic coordinates(Mori et al., 2023). Superimposed contours show relative exposures. Only the very bright sources are indicated.

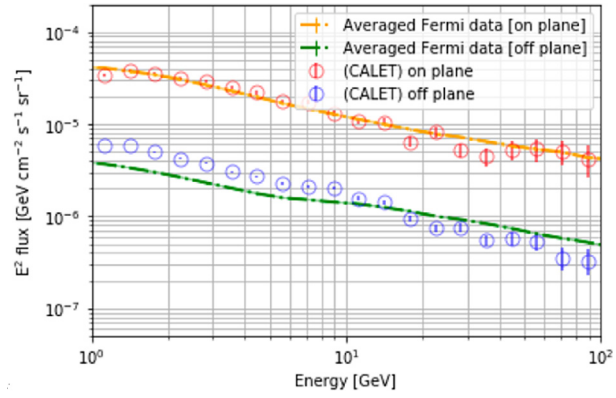

Fig. 21. The galactic plane (diffuse plus point-sources) spectra ($|l| < 80°$ & $|b| < 8°$) and the off-galactic plane spectra ($|b| > 10°$ taken with CALET for LE-γ data(Mori et al., 2023) and Fermi-LAT.

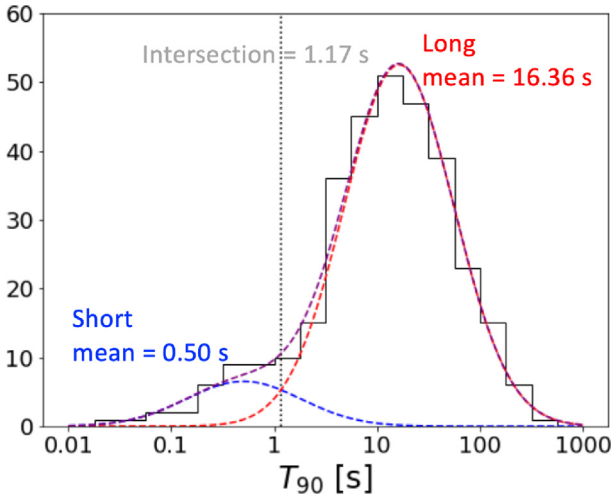

Fig. 22. Gamma-ray burst duration distribution measured by SGM (40–1000 keV).

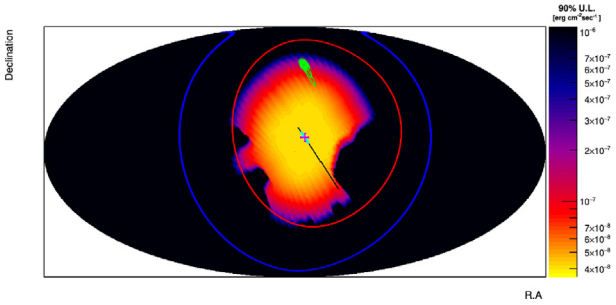

Fig. 23. 90% confidence level upper limits(Adriani et al., 2022c) observed by CAL in the energy range 1 – 10 GeV during the interval ±60 s around the time of GW 190408an reported by LIGO/Virgo. Intensity scale is given in units of erg cm^{-2} s^{-1}. Green Contour is the LIGO/Virgo high probability region. Magenta cross marks the pointing direction of CAL at T_0, and the track of the pointing direction is marked cyan broad line in the interval ±60 s. Red and blue circles are the HXM and SGM fields of view ignoring effects of the ISS structures, respectively. (For interpretation of the references to colour in this figure legend, the reader is referred to the web version of this article.)

on the high-energy gamma-ray flux were derived for 20 out of 57 events from the LIGO/Virgo third observation (O3) run (Adriani et al., 2022c). Fig. 23 shows the 90% confidence level upper limit map during the interval $T_0 = 60$s for S190408an. Upper limits were calculated for any directions in each pixel and shown as a color map.

CALET has been searching for electromagnetic counterparts in O4 as well as O3. As of the end of June 2023, the LIGO/Virgo/KAGRA collaboration reported 169 events via the GCN/LVC NOTICE, and 15 of 169 events were reported to GCN Circulars as significant events.Although CGBM and Calorimeter searched for signals associated with the significant events, no candidates were found around the event time of the significant events. We obtained the upper limits for eight significant events of which localization high probability region overlapped with the Calorimeter field of view Kawakubo et al. (2023).

4.7. Solar modulation

CALET observations of low-energy cosmic rays have been successfully performed with a Low-Energy Electron (LEE) shower trigger mode activated only at high geomagnetic latitudes (Asaoka et al., 2018). An analysis of electrons and protons to investigate the solar modulation during the descending phase of the solar cycle 24 was published in Adriani et al. (2023c), and the extended analysis to the ascending phase of the solar cycle 25, utilizing the same analysis procedure, was reported in Miyake et al. (2023).

In Fig. 24, the observed variations of electron and proton count rates at an identical average rigidity of 3.8 GV are presented. These variations show a clear charge-sign dependence of the solar modulation of galactic cosmic rays (GCR), which is consistent with the prediction of a numerical drift model of the GCR transport in the heliosphere described in Adriani et al. (2023c). It is also found that the ratio of 3.8 GV proton count rate to the neutron monitor count rate (Usoskin et al., 2001) in the ascending phase of solar cycle 25 is clearly different from that in the descending phase of cycle 24. Correlations between the electron (proton) count rate and the heliospheric environmental parameters, such as the current sheet tilt angle, are a useful tool in further developing a numerical model of solar modulation.

4.8. Space weather

In addition to the cosmic-ray observations, the upper layers of CALET (CHD) are sensitive to much lower energy (> 1 MeV) radiation events, namely relativistic electron precipitation (REP) events (Kataoka et al., 2016; Kataoka et al., 2020; Bruno et al., 2022). These REP events occur when trapped or quasi-trapped electrons in the outer radiation belt are scattered into the loss cone and are sub-

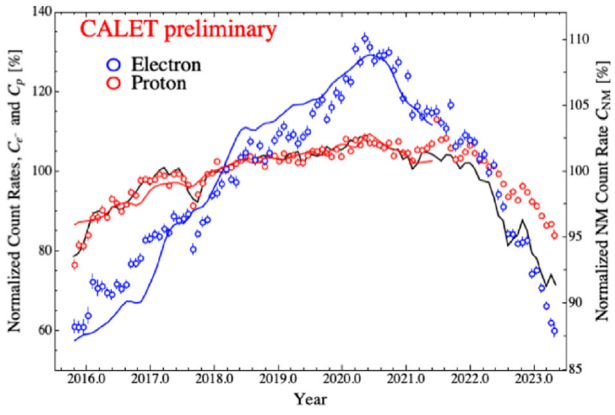

Fig. 24. Time profiles of the normalized count rates of electrons (blue open circles) and protons (red open circles) for each Carrington rotation, compared with the count rate of a neutron monitor at the Oulu station (black curve) on the right vertical axis and the electron (blue curve) and proton (red curve) count rates reproduced by the numerical drift model (Miyake et al., 2023). (For interpretation of the references to colour in this figure legend, the reader is referred to the web version of this article.)

sequently lost to the upper atmosphere (Shprits et al., 2006; Millan and Thorne, 2007), leading to the depletion of the outer radiation belt and increased bursts of radiation at low earth orbit and into the upper atmosphere.

Using the data set obtained in a period from October 2015 to October 2021, a method for the detection and categorization of MeV REP events have been studied (Ficklin et al., 2023). From this catalog, we identify a subset of a few hundred REP events observed at times where CALET is in magnetic conjunction with the Van Allen probes. These conjugate measurements enable studies of associated plasma wave data from RBSPA/B and potential drivers for MeV electron precipitation. We found that around 10 percent of REP events are coincident with enhanced electron magnetic ion cyclotron (EMIC) wave activity, suggesting that waves can play a significant role in driving MeV electron precipitation.

5. Summary and future prospects

CALET instrument performance on the ISS has been very stable during the whole scientific observation period since October 2015. During the first eight years of operation, CALET obtained new data of cosmic-ray spectra. They include a measurement of the all-electron spectrum to 7.5 TeV for searches of nearby sources and dark matter signatures, the proton spectrum to 60 TeV, and helium spectrum to 250 TeV. Cosmic-ray boron, carbon and oxygen spectra and their ratios are also updated to 3.8 TeV/n. The spectrum of iron to 1 TeV/n is updated with increased statistics by a factor of two since the last publication. The nickel spectrum is also updated. In addition, CALET has provided the data of abundance ratios of ultra heavy cosmic-ray nuclei, as well as gamma-ray measurements, GRB observations and searches of GW event counterparts. The charge-dependent solar modulation was clearly observed during the descending phase of the solar cycle 24, and the observation is extended to cycle 25. The REP observations related to space weather lead to the identification of the origin of REP.

Extended CALET operations were approved by JAXA/NASA/ASI in March 2021 through the end of 2024, and a further extension to 2030 is expected. Improved statistics and refinement of the analyses with additional data collected during the livetime of the mission will make it possible extend the measurements to higher energies and improve the spectral analyses, contributing to a better understanding of CR phenomena.

Declaration of Competing Interest

The authors declare that they have no known competing financial interests or personal relationships that could have appeared to influence the work reported in this paper.

Acknowledgements

We gratefully acknowledge JAXA's contributions to the development of CALET and to the operations onboard the International Space Station. The CALET effort in Italy is supported by ASI under Agreement No.2013–018-R.0 and its amendments. The CALET effort in the United States is supported by NASA through Grants No. 80NSSC20K0397, No. 80NSSC20K0399, and NNH18ZDA001N-APRA18-0004. This work is supported by JSPS KAKENHI Grant Nos. 19H05608 and 21K03592 in Japan.

References

Abdollahi, S., Ackermann, M., Ajello, M., et al.The Fermi-LAT Collaboration, 2017. Cosmic-ray electron-positron spectrum from 7GeV to 2TeV with the fermi large area telescope. Phys. Rev. D 95, 082007. https://doi.org/10.1103/PhysRevD.95.082007.

Adriani, O., Akaike, Y., Asano, K., et al.CALET Collaboration, 2020. Direct measurement of the cosmic-ray carbon and oxygen spectra from 10GeV/n to 2.2TeV/n with the calorimetric electron telescope on the international space station. Phys. Rev. Lett. 125, 251102. https://doi.org/10.1103/PhysRevLett.125.251102.

Adriani, O., Akaike, Y., Asano, K., et al.CALET Collaboration, 2017. Energy spectrum of cosmic-ray electron and positron from 10GeV to 3TeV observed with the calorimetric electron telescope on the international space station. Phys. Rev. Lett. 119, 181101. https://doi.org/10.1103/PhysRevLett.119.181101.

Adriani, O., Akaike, Y., Asano, K., et al.CALET Collaboration, 2022a. Observation of spectral structures in the flux of cosmic-ray protons from 50GeV to 60TeV with the calorimetric electron telescope on the international space station. Phys. Rev. Lett. 129, 101102. https://doi.org/10.1103/PhysRevLett.129.101102.

Adriani, O., Akaike, Y., Asano, K., et al.CALET Collaboration, 2022b. Direct measurement of the nickel spectrum in cosmic rays in the energy range from 8.8GeV/n to 240GeV/n with calet on the international space station. Phys. Rev. Lett. 128, 131103. https://doi.org/10.1103/PhysRevLett.128.131103.

Adriani, O., Akaike, Y., Asano, K., et al.CALET Collaboration, 2022c. Calet search for electromagnetic counterparts of gravitational waves during the ligo/virgo o3 run. Astrophys. J. 933 (1), 85. https://doi.org/10.3847/1538-4357/ac6f53.

Adriani, O., Akaike, Y., Asano, K., et al.CALET Collaboration, 2021. Measurement of the iron spectrum in cosmic rays from 10GeV/n to 2.0TeV/n with the calorimetric electron telescope on the international space station. Phys. Rev. Lett. 126, 241101. https://doi.org/10.1103/PhysRevLett.126.241101.

Adriani, O., Akaike, Y., Asano, K., et al.CALET Collaboration, 2023a. Direct measurement of the spectral structure of cosmic-ray Electrons + Positrons in the tev region with calet on the international space station. Phys. Rev. Lett. 131, 191001. https://doi.org/10.1103/PhysRevLett.131.191001.

Adriani, O., Akaike, Y., Asano, K., et al.CALET Collaboration, 2023b. Direct measurement of the cosmic-ray helium spectrum from 40GeV to 250TeV with the calorimetric electron telescope on the international space station. Phys. Rev. Lett. 130, 171002. https://doi.org/10.1103/PhysRevLett.130.171002.

Adriani, O., Akaike, Y., Asano, K., et al.CALET Collaboration, 2022d. Cosmic-ray boron flux measured from 8.4GeV/n to 3.8TeV/n with the calorimetric electron telescope on the international space station. Phys. Rev. Lett. 129, 251103. https://doi.org/10.1103/PhysRevLett.129.251103.

Adriani, O., Akaike, Y., Asano, K., et al.CALET Collaboration, 2023c. Charge-sign dependent cosmic-ray modulation observed with the

calorimetric electron telescope on the international space station. Phys. Rev. Lett. 130, 211001. https://doi.org/10.1103/PhysRevLett.130.211001.
Adriani, O., Barbarino, G.C., Bazilevskaya, G.A., et al., 2011. Pamela measurements of cosmic-ray proton and helium spectra. Science 332 (6025), 69–72. https://doi.org/10.1126/science.1199172.
Adriani, O., Barbarino, G.C., Bazilevskaya, G.A., et al., 2014. Measurement of boron and carbon fluxes in cosmic rays with the pamela experiment. Astrophys J 791 (2), 93. https://doi.org/10.1088/0004-637X/791/2/93.
Agostinelli, S., Allison, J., Amako, K., et al., 2003. Geant4—a simulation toolkit. Nucl. Instrum. Methods Phys. Res., Sect. A 506 (3), 250–303. https://doi.org/10.1016/S0168-9002(03)01368-8.
Aguilar, M., Aisa, D., Alpat, B., et al.AMS Collaboration, 2015a. Precision measurement of the proton flux in primary cosmic rays from rigidity 1GV to 1.8TV with the alpha magnetic spectrometer on the international space station. Phys. Rev. Lett. 114, 171103. https://doi.org/10.1103/PhysRevLett.114.171103.
Aguilar, M., Aisa, D., Alpat, B., et al.AMS Collaboration, 2015b. Precision measurement of the helium flux in primary cosmic rays of rigidities 1.9GV to 3TV with the alpha magnetic spectrometer on the international space station. Phys. Rev. Lett. 115, 211101. https://doi.org/10.1103/PhysRevLett.115.211101.
Aguilar, M., Ali Cavasonza, L., Alpat, B., et al.AMS Collaboration, 2017. Observation of the identical rigidity dependence of he, c, and o cosmic rays at high rigidities by the alpha magnetic spectrometer on the international space station. Phys. Rev. Lett. 119, 251101. https://doi.org/10.1103/PhysRevLett.119.251101.
Aguilar, M., Ali Cavasonza, L., Ambrosi, G., et al.AMS Collaboration, 2019. Properties of cosmic helium isotopes measured by the alpha magnetic spectrometer. Phys. Rev. Lett. 123, 181102. https://doi.org/10.1103/PhysRevLett.123.181102.
Aguilar, M., Ali Cavasonza, L., Ambrosi, G., et al.AMS Collaboration, 2021a. The alpha magnetic spectrometer (ams) on the international space station: Part ii — results from the first seven years. Phys. Rep. 894, 1–116. https://doi.org/10.1016/j.physrep.2020.09.003.
Aguilar, M., Cavasonza, L.A., Allen, M.S., et al.AMS Collaboration, 2021bs. Properties of iron primary cosmic rays: Results from the alpha magnetic spectrometer. Phys. Rev. Lett. 126, 041104. https://doi.org/10.1103/PhysRevLett.126.041104.
Ahn, H., Allison, P., Bagliesi, M., et al., 2008. Measurements of cosmic-ray secondary nuclei at high energies with the first flight of the cream balloon-borne experiment. Astropart. Phys. 30 (3), 133–141. https://doi.org/10.1016/j.astropartphys.2008.07.010.
Ahn, H.S., Allison, P., Bagliesi, M.G., et al., 2009. Energy spectra of cosmic-ray nuclei at high energies. Astrophys J 707 (1), 593. https://doi.org/10.1088/0004-637X/707/1/593.
Akaike, Y. et al. (CALET Collaboration) (2015). Simulations for calet energy calibration confirmed uisng cern-sps beam tests. Proc. Sci. (ICRC2015), (613). URL: https://articles.adsabs.harvard.edu/pdf/2013ICRC...33.2162A.
Alemanno, F., Altomare, C., An, Q., et al.DAMPE Collaboration, 2022. Detection of spectral hardenings in cosmic-ray boron-to-carbon and boron-to-oxygen flux ratios with dampe. Science Bulletin 67 (21), 2162–2166. https://doi.org/10.1016/j.scib.2022.10.002.
Alemanno, F., An, Q., Azzarello, P., et al.DAMPE Collaboration, 2021. Measurement of the cosmic ray helium energy spectrum from 70GeV to 80TeV with the dampe space mission. Phys. Rev. Lett. 126, 201102. https://doi.org/10.1103/PhysRevLett.126.201102.
Ambrosi, G., An, Q., Asfandiyarov, R., et al., 2017. Direct detection of a break in the teraelectronvolt cosmic-ray spectrum of electrons and positrons. Nature 552 (7683), 63–66. https://doi.org/10.1038/nature24475.
An, Q., Asfandiyarov, R., Azzarello, P., et al.DAMPE Collaboration, 2019. Measurement of the cosmic ray proton spectrum from 40GeV to 100TeV with the dampe satellite. Science. Advances 5 (9), eaax3793. https://doi.org/10.1126/sciadv.aax3793.
Asaoka, Y., Akaike, Y., Komiya, Y., et al., 2017. Energy calibration of calet onboard the international space station. Astropart. Phys. 91, 1–10. https://doi.org/10.1016/j.astropartphys.2017.03.002.
Asaoka, Y., Ozawa, S., Torii, S., et al., 2018. On-orbit operations and offline data processing of calet onboard the iss. Astropart. Phys. 100, 29–37. https://doi.org/10.1016/j.astropartphys.2018.02.010.
Ave, M., Boyle, P.J., Gahbauer, F., et al., 2008. Composition of primary cosmic-ray nuclei at high energies. Astrophys J 678 (1), 262. https://doi.org/10.1086/529424.
Binns, W.R., Wiedenbeck, M.E., von Rosenvinge, T.T., et al., 2022. The isotopic abundances of galactic cosmic rays with atomic number $29 \leq z \leq 38$. Astrophys J 936 (1), 13. https://doi.org/10.3847/1538-4357/ac82e7.
Böhlen, T., Cerutti, F., Chin, M., et al., 2014. The fluka code: Developments and challenges for high energy and medical applications. Nucl. Data Sheets 120, 211–214. https://doi.org/10.1016/j.nds.2014.07.049.
Bruno, A., Blum, L.W., de Nolfo, G.A., et al., 2022. Emic-wave driven electron precipitation observed by calet on the international space station. Geophys. Res. Lett. 49 (6). https://doi.org/10.1029/2021GL097529, e2021GL097529.
Cannady, N., Asaoka, Y., Satoh, F., et al., 2018. Characteristics and performance of the calorimetric electron telescope (calet) calorimeter for gamma-ray observations. Astrophys. J. Suppl. Ser. 238 (1), 5. https://doi.org/10.3847/1538-4365/aad6a3.
Engelmann, J.J., Ferrando, P., Soutoul, A., et al., 1990. Charge composition and energy spectra of cosmic-ray nuclei for elements from be to ni - results from heao-3-c2. Astron. Astrophys. 233, 96–111, URL: https://articles.adsabs.harvard.edu/pdf/1990A%26A...233...96E.
Evoli, C., Gaggero, D., Vittino, A., et al., 2017. Cosmic-ray propagation with dragon2: I. numerical solver and astrophysical ingredients. J. Cosmol. Astropart. Phys. 2017 (02), 015. https://doi.org/10.1088/1475-7516/2017/02/015.
Ferrari, A., Sala, P., Fasso, A. et al. (2005). Fluka: a multi-particle transport code. Technical Report SLAC-R-773 CERN.
Ficklin, A.W., Bruno, A., deNolfo, G., et al.CALET Collaboration, 2023. Statistical analysis into the dribers behind relativistic electron precipitation events observed by calet on the international space station. Proc. Sci. 176. https://doi.org/10.22323/1.444.0176, ICRC2023.
Fornieri, O., Gaggero, D., Grasso, D., 2020. Features in cosmic-ray lepton data unveil the properties of nearby cosmic accelerators. J. Cosmol. Astropart. Phys. 2020 (02), 009. https://doi.org/10.1088/1475-7516/2020/02/009.
Grebenyuk, V., Karmanov, D., Kovalev, I. et al. (2018). Cosmic ray nickel nuclei spectrum by the nucleon experiment. arXiv:1809.07285.
Kasahara, K., 1995. Introduction to cosmos and some relevance to ultra high energy cosmic ray air showers. Proc. of ICRC 1995 (1), 399, URL: http://adsabs.harvard.edu/full/1995ICRC....1.399K.
Kataoka, R., Asaoka, Y., Torii, S., et al., 2020. Plasma waves causing relativistic electron precipitation events at international space station: Lessons from conjunction observations with arase satellite. Journal of Geophysical Research: Space Physics 125 (9). https://doi.org/10.1029/2020JA027875, e2020JA027875.
Kataoka, R., Asaoka, Y., Torii, S., et al., 2016. Relativistic electron precipitation at international space station: Space weather monitoring by calorimetric electron telescope. Geophys. Res. Lett. 43 (9), 4119–4125. https://doi.org/10.1002/2016GL068930.
Kawakubo, Y., Cherry, M., others et al. (CALET Collaboration) (2023). Calet search for electromagnetic counterparts of gravitational wave in o4. Proc. Sci. (ICRC2023), (1517). doi:10.22323/1.444.1517.
Kawakubo, Y. et al. (CALET Collaboration) (2021). Gamma-ray burst observation & gravitational wave event follow-up with calet on the international space station. Proc. Sci. (ICRC2021), (0957). doi:10.22323/1.395.0957.
Kobayashi, K., Marrocchesi, P.S. et al. (CALET Collaboration) (2023). Observation of spectral structures in the flux of cosmic ray protons

with calet on the international space station. Proc. Sci. (ICRC2023), (092). doi:10.22323/1.444.0092.

Kobayashi, T., Komori, Y., Yoshida, K., et al., 2004. The most likely sources of high-energy cosmic-ray electrons in supernova remnants. Astrophys J 601 (1), 340. https://doi.org/10.1086/380431.

Maestro, P., Akaike, Y. et al. (CALET Collaboration) (2023). Boron flux in cosmic rays and its flux ratio to primary species measured with calet on the international space station. Proc. Sci. (ICRC2023), (058). doi:10.22323/1.444.0058.

Marrocchesi, P., Adriani, O., Akaike, Y., et al., 2011. Beam test performance of a scintillator-based detector for the charge identification of relativistic ions. Nucl. Instrum. Methods Phys. Res., Sect. A 659 (1), 477–483. https://doi.org/10.1016/j.nima.2011.08.034.

Millan, R., Thorne, R., 2007. Review of radiation belt relativistic electron losses. J. Atmos. Solar Terr. Phys. 69 (3), 362–377. https://doi.org/10.1016/j.jastp.2006.06.019.

Minagawa, G., 1981. The abundances and energy spectra of cosmic ray iron and nickel at energies from 1 to 10GeV per amu. Astrophys. J. 248, 847–855. https://doi.org/10.1086/159210.

Miyake, S., Munakata, K., Akaike, Y. et al. (CALET Collaboration) (2023). Cosmic-ray modulation during solar cycle 24–25 transition observed with calet on the international space station. Proc. Sci. (ICRC2023), (1253). doi:10.22323/1.444.1253.

Mori, M., Cannady, N. et al. (CALET Collaboration) (2023). Results from calorimetric electron telescope (calet) observations of gamma-rays on the international space station. Proc. Sci. (ICRC2023), (708). doi:10.22323/1.444.0708.

Motz, H. et al.CALET Collaboration, 2021. Investigating the vela snr's emission of electron cosmic rays with calet at the international space station. Proc. Sci. ICRC2021), (100. https://doi.org/10.22323/1.395.0100.

Mueller, D., Swordy, S.P., Meyer, P., et al., 1991. Energy spectra and composition of primary cosmic rays. Astrophys. J. 374, 356. https://doi.org/10.1086/170125.

Nishimura, J., Fujii, M., Taira, T., et al., 1980. Emulsion chamber observations of primary cosmic-ray electrons in the energy range 30 - 1000GeV. Astrophys. J. 238 (1), 394–409. https://doi.org/10.1086/157997.

Obermeier, A., Boyle, P., Hörandel, J., et al., 2012. The boron-to-carbon abundance ratio and galactic propagation of cosmic radiation. Astrophys J 752 (1), 69. https://doi.org/10.1088/0004-637X/752/1/69.

Panov, A.D., Adams, J.H., Ahn, H.S., et al., 2009. Energy spectra of abundant nuclei of primary cosmic rays from the data of atic-2 experiment: Final results. Bulletin of the Russian Academy of Sciences: Physics 73 (5), 564–567. https://doi.org/10.3103/S1062873809050098.

Roesler, S., Engel, R., Ranft, J., 2001. The monte carlo event generator dpmjet-iii. In: Kling, A., Barão, F.J.C., Nakagawa, M., Távora, L., Vaz, P. (Eds.), Advanced Monte Carlo for Radiation Physics, Particle Transport Simulation and Applications. Springer, Berlin Heidelberg, Berlin, Heidelberg, pp. 1033–1038.

Shprits, Y.Y., Li, W., Thorne, R.M., 2006. Controlling effect of the pitch angle scattering rates near the edge of the loss cone on electron lifetimes. Journal of Geophysical Research: Space Physics 111 (A12). https://doi.org/10.1029/2006JA011758.

Stolzi, F., Checchia, C., Bigongiari, G. et al. (CALET Collaboration) (2023). Iron and nickel fluxes measured by calet on the international space station. Proc. Sci. (ICRC2023), (061). doi:10.22323/1.444.0061.

Swordy, S.P., Mueller, D., Meyer, P., et al., 1990. Relative abundances of secondary and primary cosmic rays at high energies. Astrophys. J. 349, 625. https://doi.org/10.1086/168349.

Torii, S., Marrocchesi, P.S., 2019. The calorimetric electron telescope (calet) on the international space station. Adv. Space Res. 64 (12), 2531–2537. https://doi.org/10.1016/j.asr.2019.04.013.

Usoskin, I., Mursula, K., Kangas, J., et al., 2001. On-line database of cosmic ray intensities. Proc of ICRC 2001 (9), 3842, URL: https://cosmicrays.oulu.fi/ICRCNMdb.pdf.

Walsh, N.E., Akaike, Y., Binns, W.R., et al., 2022. Supertiger instrument abundances of galactic cosmic rays for the charge interval $41 \leq z \leq 56$. Adv. Space Res. 70 (9), 2666–2673. https://doi.org/10.1016/j.asr.2022.04.063.

Yoon, Y.S., Ahn, H.S., Allison, P.S., et al., 2011. Cosmic-ray proton and helium spectra from the first cream flight. Astrophys J 728 (2), 122. https://doi.org/10.1088/0004-637X/728/2/122.

Yoon, Y.S., Anderson, T., Barrau, A., et al., 2017. Proton and helium spectra from the cream-iii flight. Astrophys J 839 (1), 5. https://doi.org/10.3847/1538-4357/aa68e4.

Young, J.S., Freier, P.S., Waddington, C.J., et al., 1981. The elemental and isotopic composition of cosmic rays: Silicon to nickel. Astrophys. J. 246, 1014–1030. https://doi.org/10.1086/158997.

Zober, W.V., 2023. Abundances of ultra-heavy cosmic ray nuclei with calet. Washington University in St. Louis. https://doi.org/10.7936/t421-m924, Doctral dissertation.

Zober, W.V., Rauch, B.F. et al. (CALET Collaboration) (2023). Results of the ultra-heavy cosmic-ray analysis with calet on the international space station. Proc. Sci. (ICRC2023), (088). doi:10.22323/1.444.0088.

Zober, W.V. et al.CALET Collaboration, 2021. Progress on ultra-heavy cosmic-ray analysis with calet on the international space station. Proc. Sci. 124. https://doi.org/10.22323/1.395.0124, ICRC2021.